IEEE Access
Multidisciplinary | Rapid Review | Open Access Journal

Received March 6, 2020, accepted March 17, 2020, date of publication March 24, 2020, date of current version April 8, 2020.

Digital Object Identifier 10.1109/ACCESS.2020.2982934

Analytical Prediction and Analysis of Electromagnetic-Thermal Fields in PM Eddy Current Couplings With Injected Harmonics Into Magnet Shape for Torque Improvement

DI ZHENG AND XIFENG GUO
School of Information and Control Engineering, Shenyang Jianzhu University, Shenyang 110168, China
Corresponding author: Xifeng Guo (guoxfsjzu@163.com)

This work was supported in part by the National Key Research and Development Program of China under Grant 2019YFF0301505, and in part by the Natural Science Foundation of Liaoning Province under Grant 2019-ZD-0682.

ABSTRACT To improve the output torque in permanent magnet (PM) eddy current couplings, a new structure based on harmonics injection into the magnet optimization theory is proposed. Then, a novel analytical electromagnetic-thermal model is established that can accurately reflect the 3-D distributions of the magnetic field and the eddy current. With the proposed analytical model, the eddy current loss, temperature distribution, torque characteristics and influence of the temperature rise caused by load increases on the torque are predicted and analyzed precisely. The maximum output torque can be improved by 11.22% with injected harmonics into the magnet shape. On this basis, an optimal design of the conductor plate structure is presented, based on the electromagnetic-thermal analytical model. An additional 13.05% torque improvement can be obtained, which leads to better torque characteristics and overload capability. Verification is conducted by a 3-D finite element analysis and measurements. The analytical model solves the multiphysics coupling analysis problem of PM eddy current couplings, and provides a fast and accurate calculation method to perform electromagnetic-thermal coupling analysis.

INDEX TERMS PM eddy current couplings, torque improvement, eddy current loss, electromagnetic-thermal model.

I. INTRODUCTION

As an emerging flexible energy-saving transmission device, the PM eddy current coupling can realize torque transmission without rigid contacts and mechanical connections, which changes the operational mode of traditional mechanical transmission [1]–[3]. The structure of PM eddy current couplings cleverly utilizes the interaction between the conductor and the PM to flexibly transfer torque and energy through the electromagnetic field in the air gap. PM eddy current couplings are widely used in fan and pump equipment transmission systems of the steel, energy, military industries and other sectors [4]–[6]. Torque improvement is extremely critical during the design stage and greatly influences torque quality. In addition, the highly complex research on the PM eddy current coupling is to solve the coupling problem of electromagnetic-thermal multiphysics fields.

For PM eddy current couplings, torque modeling analysis has always been the focus of research [7]–[14]. By comparison, torque improvement studies have been insufficient until now. In recent years, optimizing the PM shape to reduce the harmonic content in the air gap magnetic density has gradually become the method used to increase the output torque of PM devices. In [15], the optimal third harmonic was injected into the sinusoidal PM shape, to improve the output torque of five-phase surface-mounted PM machines. In [16], the optimal harmonics of different orders were injected into the PM shape to maximize the output torque of five-phase machines. In [17], all rank harmonics were introduced into the PM for torque improvement, and a new design method for surface-mounted PM machines was presented. In this paper, a design method of PM eddy current couplings based

The associate editor coordinating the review of this manuscript and approving it for publication was Kan Liu.

on injected harmonics into the magnet shape is proposed to improve the output torque.

The working principle of PM eddy current couplings is that the induced eddy current generates torque directly, which leads to eddy current loss and a consequent rise in temperature. In addition, most existing works ignore thermal analysis, which results in an overheating problem that will cause the irreversible demagnetization of PMs, especially in the case of higher slip speeds. Therefore, in the PM eddy current coupling design process, a reliable theoretical model for predicting the electromagnetic-thermal performance is desirable. Unfortunately, this is a difficult task because the strong interactions of multiphysics fields lead to mathematical difficulties. Research on electromagnetic-thermal analysis of PM eddy current couplings has been insufficient until now and remains in an exploration stage. In [18], an electromagnetic-thermal analytical model was established to calculate the eddy current loss and to predict the copper plate temperature for low slip speeds. In [19], a performance study of PM eddy current couplings was presented by the electromagnetic-thermal coupling simulation with a 3-D finite model. In [20], a design optimization of axial-flux eddy current couplings was presented based on an electromagnetic–thermal model. In our previous work [21] and [22], the electromagnetic–thermal analytical models were proposed, based on a quasi 3-D electromagnetic field analytical model and a thermal resistance network model. However, the accuracy of the quasi 3-D analytical model greatly depends on the precision of the sub-loop calculation. On the other hand, this model cannot analyze the 3-D distribution of the eddy current, because of ignoring the component in the θ direction, which leads to the need for a correction factor.

There are two major objectives of this study. First, to improve the output torque, a new structure of the PM eddy current coupling based on harmonics injection into the magnet optimization theory is proposed, which essentially enhances the sinusoid of the air gap magnetic density. Second, a novel electromagnetic-thermal analytical model is established that can reflect the 3-D distributions of the magnetic field and the eddy current. Using the proposed coupling analytical model, the gradient conductor plate structure parameter is optimized to obtain the maximum output torque. In addition, the eddy current loss, temperature distribution, torque characteristics and influence of the temperature rise caused by load increases on the torque are analyzed accurately. Verification is conducted with a comparison of the analytical predicted results with those obtained from a 3-D finite element model (FEM) and measurements. This process offers satisfactory results.

II. DESCRIPTION OF NOVEL TOPOLOGY

A schematic of the PM eddy current coupling with injected harmonics into the magnet shape is shown in Fig. 1. The device consists of two parts: a PM rotor and a conductor rotor. Different from the conventional structure [7], optimized proportions of 3rd, 5th, and 7th harmonics are added to the

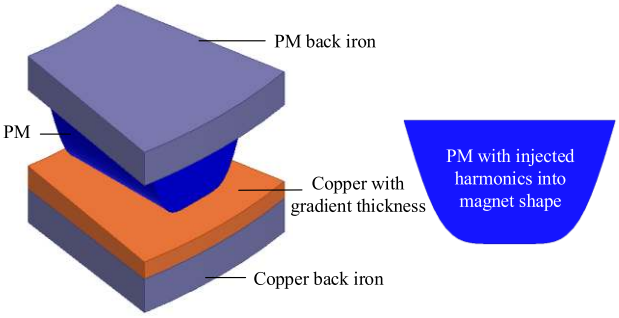

FIGURE 1. Geometry of the PM eddy current coupling with injected harmonics into the magnet shape.

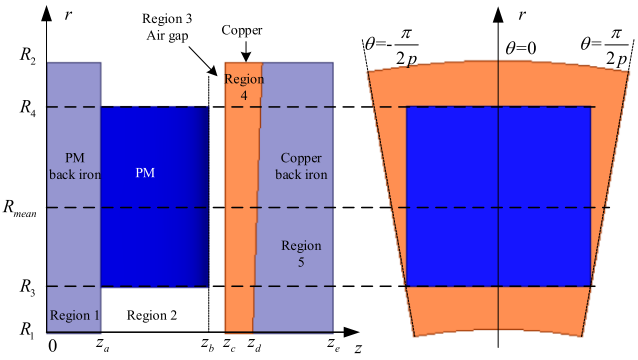

FIGURE 2. Analytical model of the PM eddy current coupling with injected harmonics into the magnet shape.

sinusoidal magnet poles, which reduces the harmonic content in the air gap magnetic density by optimizing the shape of the PM. On the other hand, considering the path of the eddy current and the penetration depth of the eddy current density, the thickness of the proposed copper plate is gradually changed. The design method can essentially enhance the sinusoid of the air gap magnetic density and greatly improve the output torque.

The analytical model is established in 3-D cylindrical coordinate. The five-layer analytical model is shown in Fig. 2. The analytical model is divided into five regions, namely, the PM back iron (region 1), the PM (region 2), the air gap (region 3), the copper (region 4), the copper back iron (region5).

PM with injected harmonics is shown in Fig. 3, the expression of PM magnetization is $\mathbf{M} = M_z(\theta)\mathbf{e_z}$, in the $z\theta$ plane.

$$M_z(\theta) = \frac{B_r}{\mu_0}(\sin(p\theta) + a_3\sin(3p\theta) + a_5\sin(5p\theta) + a_7\sin(7p\theta)) \quad (1)$$

where a_3, a_5, a_7 are the ratios of the injected 3rd, 5th, and 7th harmonics to the fundamental one.

The thickness of the proposed copper plate decreases with increasing radius, in the rz plane shown in Fig. 4. The gradient thickness of the proposed copper plate is $|z_d(\delta)| = H - (R_2 - R_1)\tan\delta$, where H is the thickness at the inner radius of the copper plate, R_1 and R_2 are the inner radius and outer radius of the copper, respectively.

In order to simplify the analysis, the main assumptions are as follows.

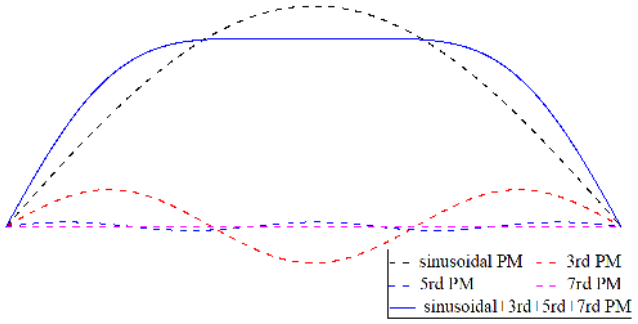

FIGURE 3. PM with injected harmonics.

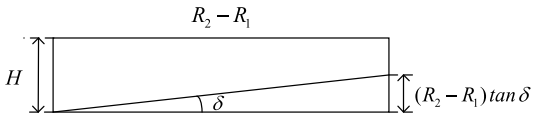

FIGURE 4. Plan view of the copper plate in the *rz* plane.

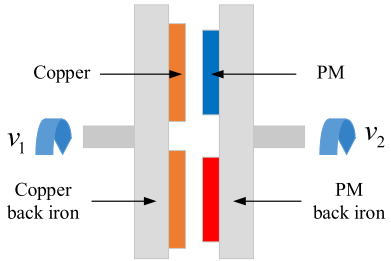

FIGURE 5. Structure of the PM eddy current coupling.

(1) The eddy current coupling operates in the steady state. v is the slip speed between the two plates ($v = v_1 - v_2$), shown in Fig. 5;

(2) The relative permeability of the PM and the copper plate equals to 1;

(3) The back iron is composed of linear media.

III. ELECTROMAGNETIC FIELD CALCULATION

For the PM back region, the PM region and the air gap region, there is no current distribution, i.e. $\mathbf{J} = 0$, the Maxwell's equation is

$$\nabla \times \mathbf{H} = 0 \tag{2}$$

Therefore, the magnetic field strength $\mathbf{H}$ can be written in terms of a magnetic potential φ_m, as

$$\mathbf{H} = -\nabla\varphi_m \tag{3}$$

The Laplace's equation of the magnetic potential $\varphi_{m,l}(l = 1, 2, 3)$ from region 1 to region 3 is

$$\frac{\partial^2\varphi_{m,l}}{\partial r^2} + \frac{1}{r}\frac{\partial\varphi_{m,l}}{\partial r} + \frac{1}{r^2}\frac{\partial^2\varphi_{m,l}}{\partial\theta^2} + \frac{\partial^2\varphi_{m,l}}{\partial z^2} = 0 \tag{4}$$

For the copper region and the copper back region, in the magnetic quasi-static field MQS analysis, there is

$$\nabla \times \mathbf{H} = \mathbf{J} + \frac{\partial\mathbf{D}}{\partial t} \approx \mathbf{J} \tag{5}$$

where $\mathbf{D}$ is electric flux density.

$$\nabla \times \nabla \times \mathbf{H} = \nabla \times \mathbf{J} \tag{6}$$

Therefore, the equations are

$$\nabla^2\mathbf{H} - \mu\sigma\frac{\partial\mathbf{H}}{\partial t} = 0 \tag{7}$$

$$\nabla^2\mathbf{E} - \mu\sigma\frac{\partial\mathbf{E}}{\partial t} = 0 \tag{8}$$

where μ is the vacuum permeability, σ are the conductivity.

The current diffusion equation is

$$\nabla^2\mathbf{J} - \mu\sigma\frac{\partial\mathbf{J}}{\partial t} = 0 \tag{9}$$

For the sinusoidal steady state, there is

$$\nabla^2\mathbf{J} = j\omega\mu\sigma\mathbf{J} \tag{10}$$

In region 4 and region 5, the induced current is distributed in the $r\theta$ plane, the equation is

$$\mathbf{J} = J_r(r, \theta, z)\mathbf{e_r} + J_\theta(r, \theta, z)\mathbf{e_\theta} \tag{11}$$

Therefore, the current diffusion equations of region 4 and region 5 ($l = 4, 5$) are

$$\begin{aligned}&\frac{\partial^2 J_{r,l}}{\partial r^2} + \frac{1}{r}\frac{\partial J_{r,l}}{\partial r} + \frac{1}{r^2}\frac{\partial^2 J_{r,l}}{\partial\theta^2} + \frac{\partial^2 J_{r,l}}{\partial z^2} - \frac{2}{r^2}\frac{J_{\theta,l}}{\partial\theta} - \frac{J_{r,l}}{r^2} \\ &\quad = j\omega\mu_0\sigma_l J_{r,l} \\ &\frac{\partial^2 J_{\theta,l}}{\partial r^2} + \frac{1}{r}\frac{\partial J_{\theta,l}}{\partial r} + \frac{1}{r^2}\frac{\partial^2 J_{\theta,l}}{\partial\theta^2} + \frac{\partial^2 J_{\theta,l}}{\partial z^2} + \frac{2}{r^2}\frac{J_{r,l}}{\partial\theta} - \frac{J_{\theta,l}}{r^2} \\ &\quad = j\omega\mu_0\sigma_l J_{\theta,l}\end{aligned} \tag{12}$$

As $\nabla \cdot \mathbf{J} = 0$, the equation (11) can be written as

$$\nabla \cdot \mathbf{J} = \frac{1}{r}\frac{\partial(rJ_r)}{\partial r} + \frac{1}{r}\frac{\partial(J_\theta)}{\partial\theta} = 0 \tag{13}$$

In order to obtain simpler and decoupled partial differential equations, new functions $X_{r,l} = rJ_{r,l}$ and $X_{\theta,l} = J_{\theta,l}/r(l = 4, 5)$ are defined, the equation (12) can be written as

$$\begin{aligned}&\frac{\partial^2 X_{r,l}}{\partial r^2} + \frac{1}{r}\frac{\partial X_{r,l}}{\partial r} + \frac{1}{r^2}\frac{\partial^2 X_{r,l}}{\partial\theta^2} + \frac{\partial^2 X_{r,l}}{\partial z^2} = j\omega\mu_l\sigma_l X_{r,l} \\ &\frac{\partial^2 X_{\theta,l}}{\partial r^2} + \frac{1}{r}\frac{\partial X_{\theta,l}}{\partial r} + \frac{1}{r^2}\frac{\partial^2 X_{\theta,l}}{\partial\theta^2} + \frac{\partial^2 X_{\theta,l}}{\partial z^2} = j\omega\mu_l\sigma_l X_{\theta,l}\end{aligned} \tag{14}$$

with

$$\mu_l = \begin{cases}\mu_0, & l = 4 \\ \mu_0\mu_s, & l = 5\end{cases} \tag{15}$$

$$\sigma_l = \begin{cases}\sigma_c, & l = 4 \\ \sigma_s, & l = 5\end{cases} \tag{16}$$

where μ_0 is the vacuum permeability, μ_s is the copper back iron relative permeability, σ_c and σ_s are the conductivity of the copper and the corresponding back iron.

The mathematical expression of $\mathbf{M} = M_z(\mathrm{r}, \theta)\mathbf{e_z}$ can be expressed by Fourier's series representation, and is given by

$$M_z(r, \theta) = \sum_{n=1,3,5,7}\sum_{h=1,2,3\ldots} M_{nk}J_{np}(\alpha_h r)e^{i\beta\theta} \tag{17}$$

with

$$M_{nh} = \frac{2M_z'(\theta)}{R_2^2 J_{np+1}(\alpha_h R_2)} \int_{R_3}^{R_4} r J_{np}(\alpha_h r) dr \tag{18}$$

where $J_{np}(\alpha_h r)$ is the Bessel function, and $J_{np}(\alpha_h R_2) = 0$.

Applying the variable separation method, the general solution of the magnetic potential equation can be expressed as

$$\varphi_{m,l}(r, \theta, z) = \sum_{n=1,3,5,7} \sum_{h=1,2,3...} \varphi(z) J_{np}(\alpha_h r) e^{i\beta\theta} \tag{19}$$

with

$$\varphi(z) = G e^{\alpha_h z} + K e^{-\alpha_h z} \tag{20}$$

The general solution to the equation of X_r for region 4 and region 5, can be expressed as

$$X_{r,l}(r, \theta, z) = \sum_{n=1,3,5,7} \sum_{h=1,2,3...} X(z) J_{np}(\alpha_h r) e^{i\beta\theta} \tag{21}$$

with

$$X(z) = U e^{\lambda_h z} + V e^{-\lambda_h z} \tag{22}$$

$$\lambda_{h,l} = \begin{cases} \sqrt{\alpha_h^2 + jnp\omega\mu_0\sigma_c}, & l = 4 \\ \sqrt{\alpha_h^2 + jnp\omega\mu_0\mu_s\sigma_s}, & l = 5 \end{cases} \tag{23}$$

where ω is the slip angular speed, p is the number of PM pole pairs.

For each region, periodic boundary condition is satisfied with

$$\mathbf{H}(r, \frac{\pi}{2p}, z) = -\mathbf{H}(r, -\frac{\pi}{2p}, z) \tag{24}$$

At $r = R_2$ each region is satisfied with $\mathbf{H} \times \mathbf{e_r} = 0$. For region 4 and region 5, the eddy current in the r direction equals to $J_r(R_2, \theta, z) = 0$.

The boundary conditions are

$$\frac{\partial \varphi_{m,1}(r, \theta, z)}{\partial z} = 0 \,|_{z=0} \tag{25}$$

$$\varphi_{m,1}(r, \theta, z_a) = \varphi_{m,2}(r, \theta, z_a) \tag{26}$$

$$\mu_s \frac{\partial \varphi_{m,1}(r, \theta, z)}{\partial z} = \frac{\partial \varphi_{m,2}(r, \theta, z)}{\partial z} + M_z \,|_{z=z_a} \tag{27}$$

$$\varphi_{m,2}(r, \theta, z_b) = \varphi_{m,3}(r, \theta, z_b) \tag{28}$$

$$\frac{\partial \varphi_{m,2}(r, \theta, z)}{\partial z} - M_z = \frac{\partial \varphi_{m,3}(r, \theta, z)}{\partial z} \,|_{z=z_b} \tag{29}$$

$$\varphi_{m,3}(r, \theta, z_c) = \frac{1}{\beta^2 \sigma_c \mu_0} \frac{\partial X_{r,3}}{\partial z} \tag{30}$$

$$\frac{\partial \varphi_{m,3}(r, \theta, z)}{\partial z} = \frac{\alpha_h^2}{\beta^2 \sigma_c \mu_0} X_{r,4} \,|_{z=z_c} \tag{31}$$

$$J_{r,4} = \frac{\sigma_c}{\sigma_s} J_{r,5} \,|_{z=z_d} \tag{32}$$

$$\frac{\partial J_{r,4}}{\partial z} = \frac{\sigma_c}{\sigma_s \mu_s} \frac{\partial J_{r,5}}{\partial z} \,|_{z=z_d} \tag{33}$$

$$J_{r,5} = 0 \,|_{z=z_e} \tag{34}$$

Using the ten independent linear equations given above, the air gap magnetic potential expression can be obtained as

$$\varphi_{m,3}(r, \theta, z) = \sum_{n=1,3,5,7} \sum_{h=1,2,3...} (G_3 e^{\alpha_h z} + K_3 e^{-\alpha_h z}) J_{np}(\alpha_h r) e^{i\beta\theta} \tag{35}$$

The eddy current expressions of the copper and the copper back iron are

$$J_{r,4}(r, \theta, z) = \sum_{n=1,3,5,7} \sum_{h=1,2,3...} \frac{1}{r} (U_4 e^{\lambda_{h4} z} + V_4 e^{-\lambda_{h4} z}) J_{np}(\alpha_h r) e^{i\beta\theta} \tag{36}$$

$$J_{\theta,4}(r, \theta, z) = \sum_{n=1,3,5,7} \sum_{h=1,2,3...} \frac{i}{\beta r} (U_4 e^{\lambda_{h4} z} + V_4 e^{-\lambda_{h4} z}) (\alpha_h J_{np-1}(\alpha_h r) - \frac{\beta}{r} J_{np}(\alpha_h r)) e^{i\beta\theta} \tag{37}$$

$$J_{r,5}(r, \theta, z) = \sum_{n=1,3,5,7} \sum_{h=1,2,3...} \frac{1}{r} (U_5 e^{\lambda_{h5} z} + V_5 e^{-\lambda_{h5} z}) J_{np}(\alpha_h r) e^{i\beta\theta} \tag{38}$$

$$J_{\theta,5}(r, \theta, z) = \sum_{n=1,3,5,7} \sum_{h=1,2,3...} \frac{i}{\beta r} (U_5 e^{\lambda_{h5} z} + V_5 e^{-\lambda_{h5} z}) (\alpha_h J_{np-1}(\alpha_h r) - \frac{\beta}{r} J_{np}(\alpha_h r)) e^{i\beta\theta} \tag{39}$$

where a_1, a_2, a_3, a_4, a_5, a_6, a_7, G_3, K_3, U_4, V_4, U_5, V_5 are given in the appendix.

IV. THERMAL ANALYSIS

A. THERMAR ANALYSIS

Based on T-equivalent modeling approach, a simple equivalent thermal network model is established to conduct the thermal analysis, shown in Fig. 6. In the model, the geometry of the PM eddy current coupling is subdivided into 8 components: (1) PM, (2) PM back iron, (3) air gap, (4) aluminium, (5) copper back iron, (6) frame, (7) copper, (8) cooling fins.

In this paper, conduction heat transfer and convection heat transfer are concerned, neglecting radiation heat transfer. The general expression of conduction thermal resistances is [23]

$$R_{conduction} = \frac{L}{kA} \tag{40}$$

where L is the heat transfer path length, A is the heat flow path area, k is the material thermal conductivity.

The components of the PM eddy current coupling are approximate hollow cylindrical as shown in Fig. 7. The thermal resistances of the classical T-type thermal model can be calculated as follows. For the axial direction, the thermal resistances can be calculated from (41) and (42). For the

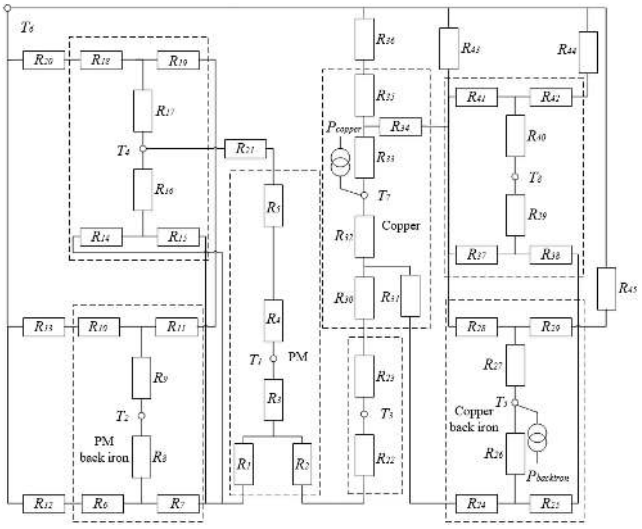

FIGURE 6. Equivalent thermal resistance network of the PM eddy current coupling.

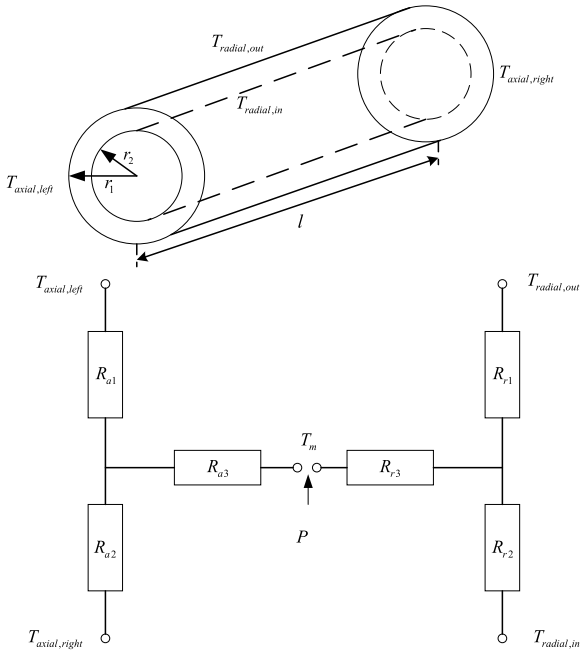

FIGURE 7. Equivalent thermal circuit of a hollow cylindrical component.

radial direction, they can be calculated from (43)-(45).

$$R_{a1} = R_{a2} = \frac{l}{2\pi k_a (r_1^2 - r_2^2)} \tag{41}$$

$$R_{a3} = \frac{-l}{6\pi k_a (r_1^2 - r_2^2)} \tag{42}$$

$$R_{r1} = \frac{1}{4\pi k_r l}\left(1 - \frac{2r_2^2 ln(r_1/r_2)}{(r_1^2 - r_2^2)}\right) \tag{43}$$

$$R_{r2} = \frac{1}{4\pi k_r l}\left(\frac{2r_2^2 ln(r_1/r_2)}{(r_1^2 - r_2^2)} - 1\right) \tag{44}$$

$$R_{r3} = \frac{-1}{8\pi k_r l(r_1^2 - r_2^2)}\left(r_1^2 + r_2^2 - \frac{4r_1^2 r_2^2 ln(r_1/r_2)}{(r_1^2 - r_2^2)}\right) \tag{45}$$

where r_1 and r_2 are the outer and inner radius of the hollow cylinder, l is the length, $T_{axial,left}$ and $T_{axial,right}$ are the temperature at both ends of the axis, $T_{radial,in}$ and $T_{radial,out}$ are the temperature of inner and outer surfaces, T_m is the component average temperature, P is the corresponding internal heat production, k_a and k_r are the thermal conductivity in the axial and radial directions respectively.

The conduction thermal resistances $R_1 - R_{11}$, $R_{14} - R_{19}$, R_{24}-R_{35} and $R_{37} - R_{42}$ can be calculated according to the thermal resistance formulations (41)-(45).

The general expression of convection thermal resistances is [24]

$$R_{convection} = \frac{1}{hA} \tag{46}$$

where h is the convection heat transfer coefficient.

For R_{12}, R_{13}, R_{20}, R_{36} and $R_{43} - R_{45}$, the heat transfer coefficient can be estimated as a function of the air speed over the surface [25]

$$h = \frac{1 + 0.25v_k}{0.045} \tag{47}$$

where v_k is the rotational speed of the surface.

For R_{22} and R_{23}, the heat transfer coefficient for the air gap is evaluated based on Nusselt number N_u [26]

$$h = \frac{N_u \lambda_{air}}{g} \tag{48}$$

$$N_u = \frac{0.3387(\frac{v_i g}{\gamma})^{1/2}(\frac{c_p v_i}{\lambda_{air}})^{1/3}}{(1 + (\frac{0.0468\lambda_{air}}{c_p v_i})^{2/3})^{1/4}} \tag{49}$$

where λ_{air} is the air thermal conductivity, g is the air gap length, γ is the air kinematic viscosity, v_i is relative velocity of two convective heat transfer surfaces, c_p is the air specific heat.

To obtain the individual node temperatures of the whole thermal model, a set of 8 steady-state heat balance equations is listed as

$$-G_{j1}T_1 - \cdots + G_{jj}T_j - \cdots - G_{jn}T_n = Q_j, \quad j = 1, \ldots, 8 \tag{50}$$

The thermal components of the thermal model are defined by MATLAB, and the temperature of each node is calculated.

B. ELECTROMAGNETIC-THERMAL MODEL CALCULATION

The calculation flowchart of the electromagnetic-thermal model is shown in Fig. 8. As the material electromagnetic and thermal characteristics change with temperature, the process of the coupling analysis is iteratively updated recalculation. Firstly, the initial structure parameters and the node temperature are set, the electromagnetic field and temperature field are analyzed respectively. The torque characteristics

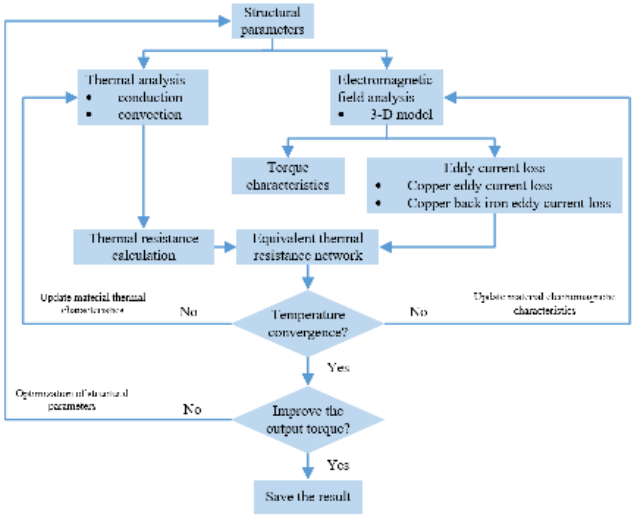

FIGURE 8. Flowchart of the electromagnetic-thermal model.

and eddy current loss are obtained by the 3-D electromagnetic field analytical model. Then, the equivalent thermal network model is used to calculate the temperature distribution, which the eddy current loss is used as the heat source for the thermal analysis. The node temperature is cycled based on the updated material electromagnetic and temperature characteristics. The iterative calculation process until the end of temperature convergence. Finally, verify whether the electromagnetic characteristics of the PM eddy current coupling with injected harmonics into the magnet shape meet the purpose of improving the output torque. If not, the structural parameters are optimized sequentially, and the electromagnetic-thermal coupling analysis calculation flow is updated, and if so, the calculation result is saved.

C. OPTIMAL DESIGN BASED ON ELECTROMAGNETIC-THERMAL COUPLING ANALYSIS

Based on the 3-D electromagnetic-thermal coupling analytical model, the gradient angle of the copper is optimized with the maximum output torque as the optimization target, ensuring that the other structural parameters are unchanged. The proposed optimization model is

$$\begin{aligned} \max: f(x) &= \frac{T(\delta)}{T_{inital}} \\ \text{s.t.}: g_1(x) &= \frac{S}{S_{inital}} = 1 \\ g_2(x) &= T_{PM} - 110 \le 0 \\ g_3(x) &= T_{copper} - 850 \le 0 \end{aligned} \tag{51}$$

where δ is the gradient angle of the copper, x is the design parameter vector, T is the torque, T_{inital} is the inital torque at $\delta = 0$, S and S_{inital} are the other structural parameters, T_{PM} is the PM temperature, T_{copper} is the copper temperature. The maximum working temperature of PM NdFeB 48H is 120°C.

TABLE 1. Specifications of the investigated coupling.

Quantity	Value
Number of poles	9
Maximum PM thickness	30 mm
Copper plate thickness	10 mm
Inner diameter (copper side)	180 mm
Outer diameter (copper side)	280 mm
Minimum air gap	3 mm
Primary side speed	1455 rpm

V. RESULTS AND DISCUSSIONS

A. SPECIFICATIONS OF THE INVESTIGATED COUPLING

Except for the PM arrangement and the thickness gradient copper, the PM eddy current coupling with injected harmonics into the magnet shape studied in this paper has the same basic structure and physical parameters as those of the one presented in [21]. The ratios of the injected third, fifth and seventh harmonics to the fundamental one are $a_3 = 1/6$, $a_5 = (3-\sqrt{5})/40$, and $a_7 = -0.0005$, as shown in Fig. 3. For the maximum output torque, the optimized gradient angle of the copper is $\delta = 2.1°$, as shown in Fig. 4. The main specifications of the investigated coupling are shown in Table 1. To test and validate the actual performance of the prototype, an experimental platform has been designed and established, and the specific details are described in our previous study [21].

B. EDDY CURRENT LOSS

At the rated slip case ($s = 0.04$), the 3-D FEM eddy current density results of the copper and the copper back iron are shown in Fig. 9. With the proposed analytical formulas (36) and (37), the eddy current density distributions of the copper along the r and θ directions are presented in Fig. 10, the component along the z direction is zero. Compared with the 3-D FEM, the induced current is well predicted by the proposed analytical model in terms of amplitudes and waveforms. With optimum injected harmonics into the magnet shape, the sinusoid of the air gap magnetic density is essentially enhanced, and the induced current distribution is quasi-sinusoidal. In the quasi 3-D analytical model in [21], the eddy current density along the θ direction is ignored, which leads to the need for a correction factor. Therefore, the 3-D analytical model can accurately analyze the 3-D distribution of eddy current density with higher calculation accuracy.

With the proposed 3-D analytical model, the eddy current loss of the copper and the copper back iron can be given by

$$\begin{aligned} P_{copper} = \frac{1}{\sigma_c}\Big(&\int_{R_1}^{R_2}\int_0^{2\pi}\int_{z_c}^{z_d} \left|J_{r,4}(r,\theta,z)\right|^2 r dr d\theta dz \\ &+ \int_{R_1}^{R_2}\int_0^{2\pi}\int_{z_c}^{z_d} \left|J_{\theta,4}(r,\theta,z)\right|^2 r dr d\theta dz\Big) \end{aligned} \tag{52}$$

$$\begin{aligned} P_{backiron} = \frac{1}{\sigma_s}\Big(&\int_{R_1}^{R_2}\int_0^{2\pi}\int_{z_d}^{z_e} \left|J_{r,5}(r,\theta,z)\right|^2 r dr d\theta dz \\ &+ \int_{R_1}^{R_2}\int_0^{2\pi}\int_{z_d}^{z_e} \left|J_{\theta,5}(r,\theta,z)\right|^2 r dr d\theta dz\Big) \end{aligned} \tag{53}$$

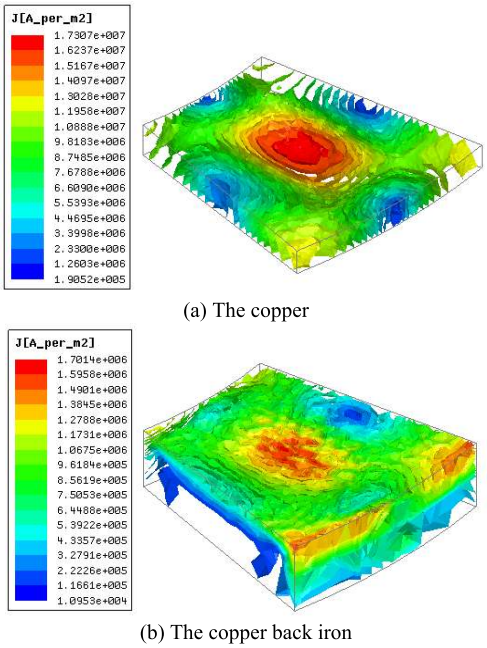

FIGURE 9. 3-D FEM eddy current density results.

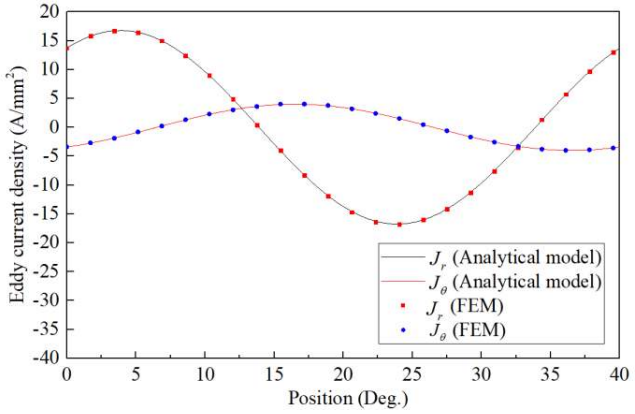

FIGURE 10. Eddy current density of the copper (at the mean radius).

As the slip increases with the load increases, the slip is selected as the variable. The eddy current loss-slip curves, obtained by the proposed 3-D analytical model, the quasi 3-D analytical model in [21], and the 3-D FEM, are shown in Fig. 11. For clarity, the eddy current loss of the copper back iron is multiplied by the coefficient. Compared with the 3-D FEM, the deviation of the quasi 3-D analytical model is under 3.76%, and the deviation of the 3-D analytical model is under 2.94%, which has higher computational accuracy.

C. TEMPERATURE DISTRIBUTION

As the symmetric structure, one pole of the PM eddy current coupling is analyzed in ANSYS Workbench 14.5. At the rated slip case, the temperature distributions of the PM and the copper are calculated, shown in Fig. 12.

Under variable loads, in the steady state the analytical result of the temperature is compared with the FEM result

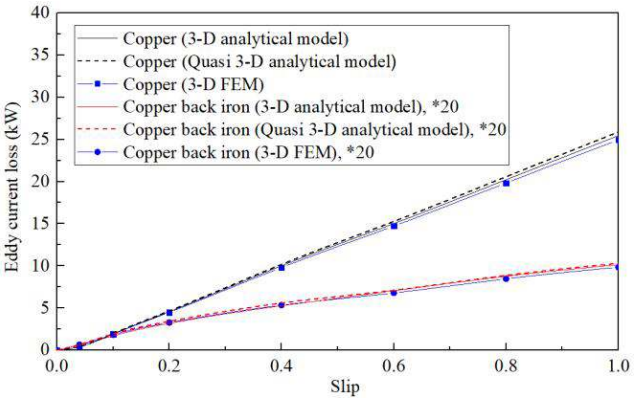

FIGURE 11. Comparison of analytical and FEM results of the eddy current loss.

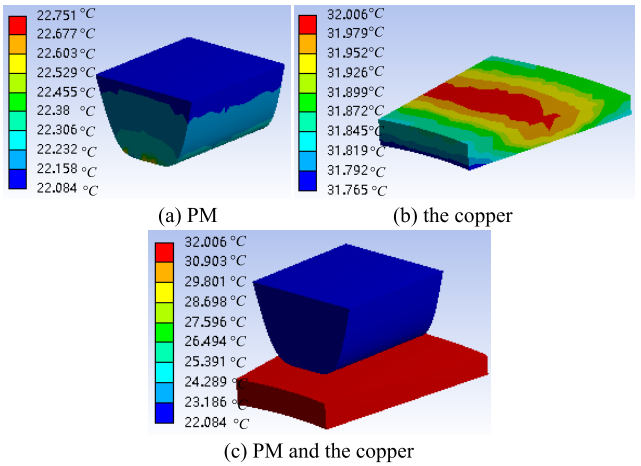

FIGURE 12. Temperature distribution by the 3-D FEM.

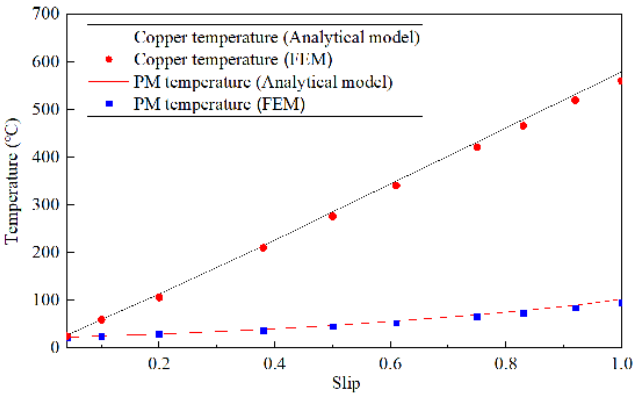

FIGURE 13. Copper and PM temperature analysis.

shown in Fig. 13. The temperature analytical calculation values of the copper and the PM can be well matched with the FEM calculation values. The comparison result shows that the analytical model is consistent with FEM and can predict the temperature accurately.

The electromagnetic-thermal analysis is considered via a temperature iteration calculation. The proposed analytical model takes much less computation time. The

electromagnetic-thermal coupling computing time is nearly all less than 15 s. However, the 3-D FEM computing time is nearly 180 min.

D. TORQUE

The magnetic field strength of the air gap is obtained from the air gap magnetic potential $\varphi_{m,3}$, and given by

$$H_{\theta 3} = -\frac{1}{r}\frac{\partial \varphi_{m,3}}{\partial \theta} = -\frac{i\beta}{r}\Big(\sum_{n=1,3,5,7}\sum_{h=1,2,3\ldots}(G_3 e^{\alpha_h z} + K_3 e^{-\alpha_h z})J_{np}(\alpha_h r)e^{i\beta\theta}\Big) \tag{54}$$

$$H_{z3} = -\frac{\partial \varphi_{m,3}}{\partial z} = \alpha_k\Big(\sum_{n=1,3,5,7}\sum_{h=1,2,3\ldots}(G_3 e^{\alpha_h z} - K_3 e^{-\alpha_h z})J_{np}(\alpha_h r)e^{i\beta\theta}\Big) \tag{55}$$

Then, the magnetic flux density of the air gap is

$$B_{\theta(3)} = -\frac{i\beta\mu_0}{r}\Big(\sum_{n=1,3,5,7}\sum_{h=1,2,3\ldots}(G_3 e^{\alpha_h z} + K_3 e^{-\alpha_h z})J_{np}(\alpha_h r)e^{i\beta\theta}\Big) \tag{56}$$

$$B_{z(3)} = \alpha_h\mu_0\Big(\sum_{n=1,3,5,7}\sum_{h=1,2,3\ldots}(G_3 e^{\alpha_h z} - K_3 e^{-\alpha_h z})J_{np}(\alpha_h r)e^{i\beta\theta}\Big) \tag{57}$$

The electromagnetic torque can be obtained from the air gap magnetic flux density. With the Maxwell stress tensor method, the electromagnetic torque is

$$T_{em} = \frac{1}{\mu_0}\int_0^{2\pi}\int_{R_1}^{R_2} r^2 B_{\theta(3)}B_{z(3)}drd\theta \tag{58}$$

where R_1 is the copper plate inner radius, R_2 is the copper plate outer radius.

The torque–slip characteristics curves, obtained by the analytical method with (58), the 3-D FEM and measurements, are shown in Fig. 14. Based on electromagnetic-thermal coupling analysis, the 3-D FEM and measurements are used to verify the proposed analytical model, and the deviation is under 4.17%.

Using the PM of the same material and volume, the torque comparison of the PM eddy current coupling with different magnet shapes is shown in Fig. 15. Compared with the typical rectangle-shaped magnet structure, the maximum torque of the injected harmonics into the magnet shape structure (at $\delta = 0°$) is increased by 11.22%, and an additional 13.05% torque improvement can be obtained with the optimized structure (at $\delta = 2.1°$). Furthermore, compared with the combined rectangle-shaped magnet structure in [21] and

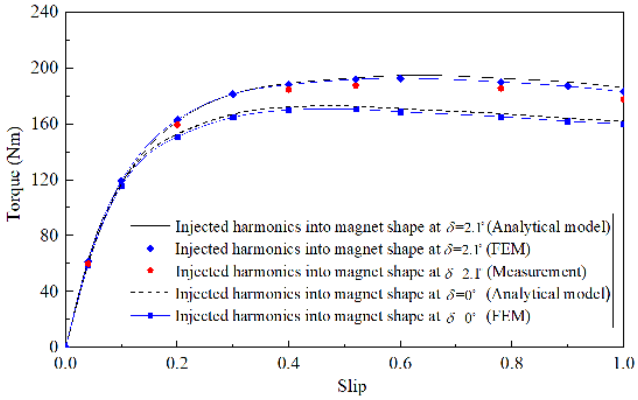

FIGURE 14. Torque-slip characteristics.

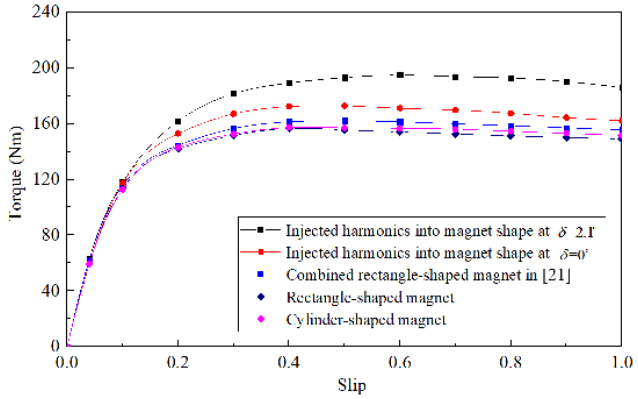

FIGURE 15. Torque comparison of the PM eddy current coupling with different magnet shapes.

the cylinder-shaped magnet structure, the maximum torque of the injected harmonics into the magnet shape structure (at $\delta = 0°$) is respectively increased by 6.78% and 9.54%. Meanwhile, 12.67% and 12.72% further more torque improvement can be respectively obtained with the optimized structure (at $\delta = 2.1°$). The torque comparison result shows that the injected harmonics into the magnet shape structure has obvious effect on torque improvement, and the optimized structure leads to better torque characteristics. It greatly improves the maximum output torque of the PM eddy current coupling.

E. EFFECT OF TEMPERATURE RISE CAUSED INCREASE ON TORQUE

For the optimized injected harmonics into the magnet shape structure, the torque-slip characteristics analysis is presented in Fig. 16. Point A is the synchronous running point, where the slip is 0. As the conductor rotor does not cut the magnetic field line of the PM rotor, the electromagnetic torque at this point is 0. Point B is the rated operating point, where the slip is 0.04, and T_B is the rated electromagnetic torque. Point C is the critical operating point, where T_C is the maximum electromagnetic torque. Point D is the blocking operation point, where the slip is 1. The PM eddy current coupling can operate stably in the AC segment. However, the CD segment is the state in which the coupling goes from critical to stalled.

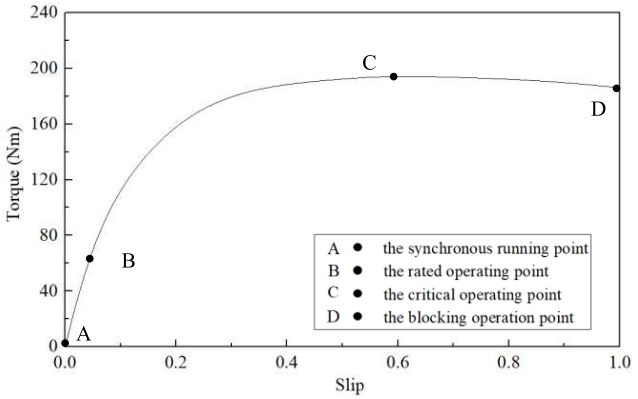

FIGURE 16. Torque-slip characteristics analysis.

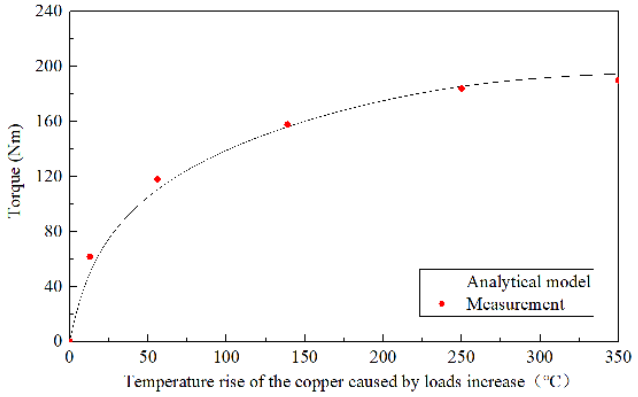

FIGURE 17. The influence of the copper temperature rise caused by loads increase on the torque.

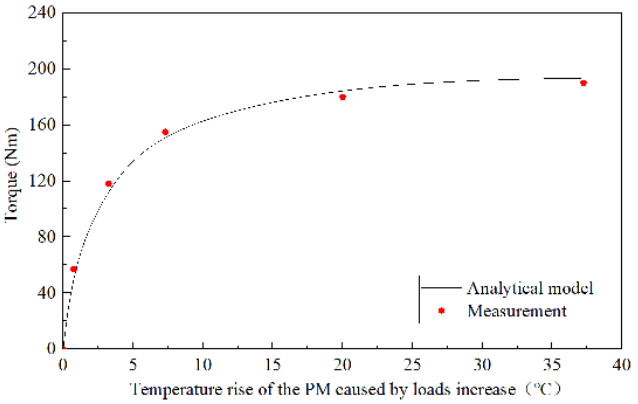

FIGURE 18. The influence of PM temperature rise caused by loads increase on the torque.

During the CD segment, the eddy current loss is too much, the temperature rise is too high, therefore the coupling can't work long.

In the AC segment, based on the electromagnetic-thermal coupling analytical model, the influence of the temperature rise of the copper and the PM caused by load increases, are shown in Fig. 17 and Fig. 18 respectively.

As a result, the objective of improving the torque characteristics is to stabilize the operating section of the AC section, enhancing the rated electromagnetic torque and the maximum electromagnetic torque. Compared with the pre-optimized structure, the rated torque of the optimized structure is increased by 4.41%, the maximum torque is increased by 13.05%, and the overload capability is increased by 8.27%. The optimized structure improves the rated torque and greatly improves the maximum output torque and overload capability of the PM eddy current coupling.

As load increases, a large amount of temperature rise is caused, and even the PM is irreversibly demagnetized. Therefore, it is of great significance to perform electromagnetic-thermal coupling analysis.

VI. CONCLUSION

In this paper, a new structure for PM eddy current couplings with injected harmonics into the magnet shape is proposed to improve the output torque. A novel electromagnetic-thermal analytical model that can accurately reflect the 3-D distribution of the magnetic field and the eddy current, is presented to analyze the eddy current loss, temperature distribution, and torque characteristics. On this basis, the gradient angle of the copper is optimized to maximize the output torque, based on the multiphysics coupling analytical model. Compared to previous analytical models, the proposed model is able to predict the effect of the temperature rise caused by load increases on the torque.

The proposed analytical model is verified by comparing the analytical predicted results with those obtained from the 3-D FEM and measurements, which provide satisfactory results. The design method proposed in this paper gives the PM eddy current coupling has better torque characteristics and overload capability. The electromagnetic-thermal analytical model proposed in this paper provides a fast and accurate calculation method for multiphysics coupling analysis of the PM eddy current coupling. Additionally, the model proposed in this paper solves the problem of multiphysics coupling analysis, ensuring that the temperature rise caused by eddy current loss does not cause irreversible demagnetization of PMs.

APPENDIX

The elements of equation (35) to equation (39) are expressed as follows.

$$a_1 = 2\alpha_h e^{\alpha_h z_a} e^{\alpha_k z_b} - e^{2\alpha_h z_a}\lambda_k\mu_s + e^{2\alpha_h z_b}\lambda_h\mu_s \tag{A.1}$$

$$a_2 = e^{2\alpha_h z_c} + e^{2\lambda_h z_d} \tag{A.2}$$

$$a_3 = e^{2\alpha_h z_c} - e^{2\lambda_h z_d} \tag{A.3}$$

$$a_4 = e^{2\lambda_h z_d} + e^{2\lambda_h z_e} \tag{A.4}$$

$$a_5 = e^{2\lambda_h z_d} - e^{2\lambda_h z_e} \tag{A.5}$$

$$a_6 = e^{2\alpha_h z_a} + e^{2\alpha_h z_c} \tag{A.6}$$

$$\begin{aligned} a_7 = {} & e^{2\alpha_h z_a}\alpha_h a_5 a_2 + e^{2\lambda_h z_d}\lambda_h a_3 a_6 - e^{2\alpha_h z_c} e^{2\lambda_h z_d}\alpha_h a_2 \\ & - e^{4\alpha_h z_c} e^{2\lambda_h z_e}(\lambda_h - \alpha_h) + e^{2\alpha_h z_c} e^{2\lambda_h z_d} e^{2\lambda_h z_e}(\lambda_h + \alpha_h) \\ & - e^{2\alpha_h z_a} e^{2\alpha_h z_c} e^{2\lambda_h z_e}\lambda_h a_3 \end{aligned} \tag{A.7}$$

$$G_3 = \frac{M_{nh} a_1 (\alpha_h a_2 a_5 + \lambda_h e^{2\alpha_h z_c} a_3 a_5)}{2 e^{\alpha_h z_b}\alpha_h \lambda_h \mu_s a_7} \tag{A.8}$$

$$K_3 = \frac{e^{2\alpha_h z_c} M_{nh} a_1 a_5 (\lambda_h a_3 - \alpha_h a_2)}{2e^{\alpha_h z_b} \alpha_h \lambda_h \mu_s a_7} \tag{A.9}$$

$$U_4 = \frac{e^{2\alpha_h z_c} M_{nh} (e^{2\alpha_h z_c} + 1) a_1 \beta^2 \sigma_c \mu_0 \omega}{2e^{\alpha_h z_b} \lambda_h \alpha_h \mu_s a_7} \tag{A.10}$$

$$V_4 = \frac{e^{2\alpha_h z_c} e^{2\lambda_h z_d} M_{nh} (e^{2\alpha_h z_c} + 1) a_1 \beta^2 \sigma_c \mu_0 \omega}{2e^{\alpha_h z_b} \lambda_h \alpha_h \mu_s a_7} \tag{A.11}$$

$$U_5 = \frac{e^{2\alpha_h z_c} e^{2\lambda_h z_d} M_{nh} \mu_s (e^{2\alpha_h z_c} + 1) a_1 \beta^2 \sigma_c \mu_0 \omega \sigma_s}{e^{\alpha_h z_b} \lambda_h \alpha_h a_7 \mu_s^2 \sigma_c} \tag{A.12}$$

$$V_5 = \frac{-e^{2\alpha_h z_c} e^{2\lambda_h z_d} e^{2\lambda_h z_e} M_{nh} \mu_s (e^{2\alpha_h z_c} + 1) a_1 \beta^2 \sigma_c \mu_0 \omega \sigma_s}{e^{\alpha_h z_b} \lambda_h \alpha_h a_7 \mu_s^2 \sigma_c} \tag{A.13}$$

REFERENCES

[1] T. Lubin and A. Rezzoug, "Steady-state and transient performance of axial-field eddy-current coupling," *IEEE Trans. Ind. Electron.*, vol. 62, no. 4, pp. 2287–2296, Apr. 2015.

[2] S. Mohammadi, M. Mirsalim, S. Vaez-Zadeh, and H. A. Talebi, "Analytical modeling and analysis of axial-flux interior permanent-magnet couplers," *IEEE Trans. Ind. Electron.*, vol. 61, no. 11, pp. 5940–5947, Nov. 2014.

[3] J. Wang and J. Zhu, "A simple method for performance prediction of permanent magnet eddy current couplings using a new magnetic equivalent circuit model," *IEEE Trans. Ind. Electron.*, vol. 65, no. 3, pp. 2487–2495, Mar. 2018.

[4] Z. Li, D. Wang, D. Zheng, and L. Yu, "Analytical modeling and analysis of magnetic field and torque for novel axial flux eddy current couplers with PM excitation," *AIP Adv.*, vol. 7, no. 10, Oct. 2017, Art. no. 105303.

[5] K.-C. Min, J.-Y. Choi, J.-M. Kim, H.-W. Cho, and S.-M. Jang, "Eddy-current loss analysis of noncontact magnetic device with permanent magnets based on analytical field calculations," *IEEE Trans. Magn.*, vol. 51, no. 11, Nov. 2015, Art. no. 8110304.

[6] H. Zhang, D. Wang, and X. Wang, "Equivalent circuit model of eddy current device," *IEEE Trans. Magn.*, vol. 54, no. 4, May 2018, Art. no. 8001009.

[7] T. Lubin and A. Rezzoug, "Improved 3-D analytical model for axial-flux eddy-current couplings with curvature effects," *IEEE Trans. Magn.*, vol. 53, no. 9, Sep. 2017, Art. no. 8002409.

[8] K. Shin, H. Park, and H. Cho, "Semi-three-dimensional analytical torque calculation and experimental testing of an eddy current brake with permanent magnets," *IEEE Trans. Appl. Supercond.*, vol. 28, no. 3, Apr. 2018, Art. no. 5203205.

[9] B. Dolisy, S. Mezani, T. Lubin, and J. Leveque, "A new analytical torque formula for axial field permanent magnets coupling," *IEEE Trans. Energy Convers.*, vol. 30, no. 3, pp. 892–899, Sep. 2015.

[10] T. Lubin and A. Rezzoug, "3-D analytical model for axial-flux eddy-current couplings and brakes under steady-state conditions," *IEEE Trans. Magn.*, vol. 51, no. 10, Oct. 2015, Art. no. 8203712.

[11] J. Wang, H. Lin, and S. Fang, "Analytical prediction of torque characteristics of eddy current couplings having a Quasi-Halbach magnet structure," *IEEE Trans. Magn.*, vol. 52, no. 6, Jun. 2016, Art. no. 8001209.

[12] M.-G. Park, J.-Y. Choi, H.-J. Shin, and S.-M. Jang, "Torque analysis and measurements of a permanent magnet type eddy current brake with a Halbach magnet array based on analytical magnetic field calculations," *J. Appl. Phys.*, vol. 115, no. 17, May 2014, Art. no. 17E707.

[13] X. Dai, Q. Liang, and J. Cao, "Analytical modeling of axial-flux permanent magnet eddy current couplings with a slotted conductor topology," *IEEE Trans. Magn.*, vol. 52, no. 2, Feb. 2016, Art. no. 8000315.

[14] J. Wang, H. Lin, S. Fang, and Y. Huang, "A general analytical model of permanent magnet eddy current couplings," *IEEE Trans. Magn.*, vol. 50, no. 1, Jan. 2014, Art. no. 8000109.

[15] K. Wang, Z. Q. Zhu, and G. Ombach, "Torque improvement of five-phase surface-mounted permanent magnet machine using third-order harmonic," *IEEE Trans. Energy Convers.*, vol. 29, no. 3, pp. 735–747, Sep. 2014.

[16] K. Wang, Z. Y. Gu, Z. Q. Zhu, and Z. Z. Wu, "Optimum injected harmonics into magnet shape in multiphase surface-mounted PM machine for maximum output torque," *IEEE Trans. Ind. Electron.*, vol. 64, no. 6, pp. 4434–4443, Jun. 2017.

[17] G. Liu, Y. Zeng, W. Zhao, and J. Ji, "Permanent magnet shape using analytical feedback function for torque improvement," *IEEE Trans. Ind. Electron.*, vol. 65, no. 6, pp. 4619–4630, Jun. 2018.

[18] D. Zheng, D. Wang, S. Li, T. Shi, Z. Li, and L. Yu, "Eddy current loss calculation and thermal analysis of axial-flux permanent magnet couplers," *AIP Adv.*, vol. 7, no. 2, Feb. 2017, Art. no. 025117.

[19] S. Wang, Y. Guo, G. Cheng, and D. Li, "Performance study of hybrid magnetic coupler based on magneto thermal coupled analysis," *Energies*, vol. 10, no. 8, p. 1148, 2017.

[20] J. Fontchastagner, T. Lubin, S. Mezani, and N. Takorabet, "Design optimization of an axial-field eddy-current magnetic coupling based on magneto-thermal analytical model," *Open Phys.*, vol. 16, no. 1, pp. 21–26, Mar. 2018.

[21] D. Zheng, D. Wang, S. Li, H. Zhang, L. Yu, and Z. Li, "Electromagnetic-thermal model for improved axial-flux eddy current couplings with combine rectangle-shaped magnets," *IEEE Access*, vol. 6, pp. 26383–26390, 2018.

[22] D. Wang, D. Zheng, S. Li, Z. Li, B. Liang, and Y. Ni, "Electromagnetic-thermal analysis of axial-flux permanent magnet eddy current couplers with sub-loop calculation method," *J. Magn.*, vol. 23, no. 4, pp. 509–516, Dec. 2018.

[23] N. Zhao, Z. Q. Zhu, and W. Liu, "Rotor eddy current loss calculation and thermal analysis of permanent magnet motor and generator," *IEEE Trans. Magn.*, vol. 47, no. 10, pp. 4199–4202, Oct. 2011.

[24] H. Li and Y. Shen, "Thermal analysis of the permanent-magnet spherical motor," *IEEE Trans. Energy Convers.*, vol. 30, no. 3, pp. 991–998, Sep. 2015.

[25] L. Li, W. N. Fu, S. L. Ho, S. Niu, and Y. Li, "A quantitative comparison study of Power-Electronic-Driven flux-modulated machines using magnetic field and thermal field co-simulation," *IEEE Trans. Ind. Electron.*, vol. 62, no. 10, pp. 6076–6084, Oct. 2015.

[26] Z. Huang, J. Fang, and X. Liu, "Loss calculation and thermal analysis of rotors supported by active magnetic bearings for high-speed permanent-magnet electrical machines," *IEEE Trans. Ind. Electron.*, vol. 63, no. 4, pp. 2027–2035, Apr. 2016.

DI ZHENG received the B.S., M.S., and Ph.D. degrees in electrical engineering from Northeastern University, Shenyang, China, in 2012, 2015, and 2019, respectively.

She is currently a Lecturer with the School of Information and Control Engineering, Shenyang Jianzhu University, Shenyang. Her current research interests include research on permanent magnet transmission theory and technology, and multiphysical field coupling analysis and modeling.

XIFENG GUO received the B.S. degree in automation, the M.S. degree in detection technology and automation from the Dalian University of Technology, Dalian, China, in 2004 and 2008, respectively, and the Ph.D. degree in power electronics and power drive from Northeastern University, Shenyang, China, in 2013.

He is currently an Associate Professor with the School of Information and Control Engineering, Shenyang Jianzhu University, Shenyang. His current research interests include the comprehensive control of building energy, research on the application of clean energy technologies, such as distributed power generation and solar energy, and research on permanent magnet transmission theory and technology.